Effects of Alumina Nanofibers and Cellulose Nanocrystals on Durability and Self-Healing Capacity of Ultrahigh-Performance Fiber-Reinforced Concretes

Estefanía Cuenca[1]; María Criado[2]; Mercedes Giménez[3]; María Cruz Alonso[4]; and Liberato Ferrara[5]

Abstract: Ultrahigh-performance fiber-reinforced concrete (UHPFRC) features outstanding durability properties in uncracked state, although its composition based on very low water/cement ratios may result in a higher risk of early-age cracking due to increased shrinkage. This paper, based on research performed in the framework of the H2020 project ReSHEALience, studied aggressive chemical exposure conditions. A UHPFRC reference mix with 0.8% crystalline admixtures (CAs) and two other mixes, one containing 0.25% alumina nanofibers (ANFs) and one containing 0.15% cellulose nanocrystals (CNCs), both by weight of cement, were investigated. This study analyzed the synergy between CA and the nanoconstituents (ANF and CNC) on the physical, chemical, mechanical, and durability properties the and self-healing capacity of uncracked and cracked UHPFRC. The results showed that the presence of nanoadditives improves the mechanical properties independently of environmental curing conditions, refines the pore structure, favors cement hydration, and improves the intrinsic durability with a Cl and water transport reduction. Moreover, in the cracked state, nanoconstituents improved the self-sealing and self-healing capacity of specimens immersed in geothermal water. **DOI: 10.1061/(ASCE)MT.1943-5533.0004375.**

Author keywords: Self-healing; Crystalline admixtures (CAs); Alumina nanofibers (ANFs); Cellulose nanocrystals (CNCs); Durability; Ultrahigh-durability concrete.

Introduction

A continuous increase in the durability requirements of the concrete structures is demanded to guarantee their safety throughout a longer service-life span, and, because of increasingly challenging environmental exposure conditions and structural service scenarios, and to reduce maintenance operations and related costs. Advanced concrete material and structure concepts, e.g., employing ultrahigh-performance fiber-reinforced concretes (UHPFRCs), are undergoing continuous progress and development. UHPFRCs can have compressive strength higher than 120–150 MPa, direct tensile strength in the range of 5–10 MPa depending on their composition and curing process, and accessible porosity below 5% (Wang et al. 2014; Shi et al. 2015; Alonso et al. 2005). The use of extremely low water/binder (w/b) ratios (generally below 0.2), a substantial amount of binder (700–1,000 kg/m^3), and a small maximum aggregate size in UHPFRC mix compositions lead to extremely compact matrixes, which are nearly impermeable to gases and water. However, the same UHPFRC composition may result in a higher risk of internal microcracking due to increased embrittlement and autogenous and drying shrinkage (Yang et al. 2019). Fibers, usually metallic fibers, are used to temper the inherent brittleness of ultrahigh-performance concrete (UHPC), creating UHPFRC. This UHPFRC also results in a one-of-a-kind tensile behavior which is characterized by multiple cracking, with significantly higher ductility and energy absorption capacity (Kusumawardaningsih et al. 2015).

RC structures are designed to work in the cracked state over their service life. An issue of concern is that cracks serve as new transport paths, in addition to the internal pore structure, that allow the entrance of aggressive environment-borne substances which can be harmful to both the cementitious matrix and the reinforcement, and seriously can compromise the durability of the structure in the long term (Li and Li 2019). In this context, self-healing technologies could prevent deterioration effects by controlling and repairing early-stage cracks, improving the durability of RC structures and increasing their service life, thus reducing the need for repairing and maintenance tasks (Ferrara et al. 2018). For this purpose, tailored additions such as crystalline admixtures recently have been used on a large scale to promote the self-healing of the cracks and the recovery of durability performance. Crystalline admixtures (CAs), a category of permeability-reducing admixture (ACI 2010), are hydrophilic materials. Their reaction with water

[1]Assistant Professor, Dept. of Civil and Environmental Engineering, Politecnico di Milano, Piazza Leonardo da Vinci 32, Milan 20133, Italy (corresponding author). ORCID: https://orcid.org/0000-0002-0810-9743. Email: estefania.cuenca@polimi.it

[2]Researcher, Dept. of Construction, Institute of Construction Science Eduardo Torroja, Calle Serrano Galvache 4, Madrid 28033, Spain. Email: maria.criado@ietcc.csic.es

[3]Ph.D. Student, Dept. of Construction, Institute of Construction Science Eduardo Torroja, Calle Serrano Galvache 4, Madrid 28033, Spain. Email: mercedes.gimenez@ietcc.csic.es

[4]Research Professor, Dept. of Construction, Institute of Construction Science Eduardo Torroja, Calle Serrano Galvache 4, Madrid 28033, Spain. ORCID: https://orcid.org/0000-0002-4308-9506. Email: mcalonso@ietcc.csic.es

[5]Associate Professor, Dept. of Civil and Environmental Engineering, Politecnico di Milano, Piazza Leonardo da Vinci 32, Milan 20133, Italy. ORCID: https://orcid.org/0000-0002-6826-9917. Email: liberato.ferrara@polimi.it

Note. This manuscript was submitted on August 14, 2021; approved on January 14, 2022; published online on May 17, 2022. Discussion period open until October 17, 2022; separate discussions must be submitted for individual papers. This paper is part of the ***Journal of Materials in Civil Engineering***, © ASCE, ISSN 0899-1561.

and with cement hydration products forms insoluble products that become part of the cement matrix, increasing the amount of calcium silicate hydrates (C—S—H) in the paste (Sisomphon et al. 2012), and precipitate that fills pores and cracks, consequently increasing the resistance to water penetration.

Despite extensive research on self-healing technologies and assessing test methods (Ferrara et al. 2018; Zhang et al. 2020), the literature on self-healing in aggressive environments still is under development, and, to the best of the authors' knowledge, is limited to chloride attack situations (Maes et al. 2016; Darquennes et al. 2016; Van Belleghem et al. 2017; Borg et al. 2018; Cuenca et al. 2021d). These studies have demonstrated that autonomous self-healing could improve concrete durability by reducing the chloride penetration through narrow cracks and preventing the chloride diffusion both along and perpendicular to these cracks (Snoeck et al. 2018).

In recent decades, extensive research also has been conducted to promote the use of nanomaterials in cementitious composites (Wu et al. 2016; Sobolev 2016; Gopalakrishnan and Jeyalakshmi 2018). Nanomaterials can significantly enhance the performance of cement-based materials given their chemical reactivity and physical filling and nucleation effects (Wu et al. 2016; Sánchez and Sobolev 2010). Their main role is to interact with the structure of the material at the nanolevel, preventing the propagation of defects at that scale and also, likely, modifying the evolution of the nanostructure. Therefore, it is reasonable to think that these materials can interact with microcracks and microdefects in concrete materials and structures from their early formation, thus preventing their growth (Sobolev 2016) and further limiting the ingress of aggressive substances, and therefore guarantying better durability of the RC over along its service life.

Whereas crystalline admixtures, as metioned previously, are minerals that deposit in the pores and capillaries of the concrete and seal the cracks, cellulose nanocrystals are expected to enhance the densification of the matrix and the matrix–aggregate interface transition zone (ITZ) (Cao et al. 2015; Kawashima and Shah 2011; Lee et al. 2018), and alumina nanofibers are considered to control the crack at nanolevel initiation and growth (e.g., Muzenski et al. 2019). In addition, the presence of alumina nanofibers in concrete has been demonstrated to enhance the matrix of cement paste (Muzenski et al. 2019; Li et al. 2006). Because of the presence of hydroxyl groups on their surface, alumina nanofibers can accelerate the hydration of cement and favor the formation of larger volumes of reaction products; they also act as filler, densifying the microstructure and leading to a reduced porosity (Gopalakrishnan and Jeyalakshmi 2018; Sánchez and Sobolev 2010; Li et al. 2006). Cellulose nanocrystals and nanofibrils have been shown to increase the density and strength of concrete and reduce shrinkage strain, bridging microcracks and filling pore spaces, thus ultimately delaying crack propagation (Cao et al. 2015; Kawashima and Shah 2011).

In the framework of aggressive environments, studies of the durability of concrete with nanoconstituents using self-healing technologies are very scarce in the literature (Cuenca et al. 2021a). In this context, this knowledge gap was the starting point for the H2020 Project ReSHEALience (Rethinking coastal defense and green Energy Service infrastructures through enHancEd durAbiLity high-performance fiber-reinforced cement-based materials) (Ferrara et al. 2019). The project aims to upgrade the UHPFRC concept by assessing the durability in the cracked stage and, in particular, whether the addition of specific functionalizing constituents (crystalline admixtures, alumina nanofibers and cellulose nanocrystals) can improve the durability in the cracked stage and the self-repairing ability.

Research Approach

As mentioned previously, the main purpose of this paper was to provide deeper insight into the intrinsic feature of the investigated ultrahigh-performance fiber-reinforced concretes in terms of their peculiar or differential microstructural characteristics, and how this affects their intrinsic durability (uncracked state) throughout the analyses of physical and mineralogical properties. The aforementioned scope was expanded through the investigation on the effects of crystalline self-healing stimulators and nanoconstituents, in the form of alumina nanofibers and cellulose nanocrystals, on the mechanical and durability performance of UHPFRCs in the cracked state, representative of real service conditions, under chemically aggressive environments.

All these findings contribute to validating the concept of ultrahigh-durability concrete (UHDC), promoted in the framework Horizon ReSHEALience project activities and conceived as an upgrading of ultrahigh-performance (fiber-reinforced) concrete due to enhanced durability in the service cracked state and under exposure to extremely aggressive conditions, which this study implemented in laboratory investigations. Moreover, the methodology employed in this paper to establish a correlation between microstructural characteristics, durability parameters, and mechanical properties also can be used effectively for the tailored design of materials intended to meet specific multiple performance demands for structural applications in specific, even extremely aggressive, scenarios.

Experimental Methodology

Materials and Mix Design Proportions

The experimental program focused on three ultrahigh-performance fiber-reinforced concretes, the composition of which is detailed in Table 1. The mixes contain an elevated amount of cement (600 kg/m^3) and a very reduced water/binder ratio (0.18) typical of ultrahigh-performance RCs. One of the aims of the paper was to

Table 1. Dosage of UHDCs

Constituents (kg/m^3)	UHDC-CA (reference)	UHDC-CA+ANF	UHDC-CA+CNC
Cement CEM I 52.5R (Buzzi Unicem, Dyckerhoff, Germany)		600	
Slag		500	
Water/(water/binder)		200/(0.18)	
Steel fibers ($l_f = 20$ mm; $d_f = 0.22$ mm) Azichem Readymix 200 (Goito, Italy)		120	
Sand (0–2 mm)		982	
Superplasticizer BASF Glenium ACE 300 (Treviso, Italy)		33	
Crystalline admixture Penetron Admix (Collegno, Italy)		4.8	
Alumina nanofibers (% by cement mass) (Nafen, Tallinn, Estonia)	0	0.25	0
Cellulose nanocrystals (% by cement mass) (API Europe, Athens, Greece)	0	0	0.15

Table 2. Composition of geothermal water

Element	Al	Ca	Fe	K	Mg	Na	S	Si	SO_4	Cl
ppm	0.2	4.0	0.1	19.8	0.3	1,243.2	1,523.4	0.3	2,678.0	440.9

analyze their mechanical and durability performance when exposed to aggressive environments, represented by geothermal water, containing chlorides (Cl = 440.9 ppm) and high contents of sulfates (SO_4 = 2,678 ppm) that classify the aggressiveness as XA; the composition of this water is presented in Table 2. These materials are defined in the ReSHEALience project as ultra high durability concretes and, therefore this name is used throughout this work. Because of the intended applications (cooling water tanks of a geothermal power plant), the reference mix (UHDC-CA) incorporated a significant amount of ground granulated blast-furnace slag (GGBS), a well-known mineral addition in conventional concretes but less common in UHPFRCs. This mineral addition contributes to refining the pores in the concrete matrix and hence enhancing its durability in combination with its ability to reduce aggressive transport as a consequence of capture and combine chlorides and sulfates, both of which are aggressive ions that were considered in this work (Kayali et al. 2012; Chen et al. 2020; Luna et al. 2018; Ozbay et al. 2016). The composition of the employed portland cement (PC) CEM I 52.5R and GGBS, as determined by X-ray fluorescence (XRF), is presented in Table 3. The main components of the PC were CaO (59.7%) and SiO_2 (19.5%), while the GGBS contained CaO (39.2%) and SiO_2 (38.9%), as well as Al_2O_3 (10.2%) that contributed to combine sulfates and chlorides. All the mixes included steel fibers (SFs) (l_f = 20 mm; d_f = 0.22 mm) at a volume fraction of 1.5% to obtain a strain-hardening tensile response at the required level of strength and deformation capacity (Lo Monte and Ferrara 2020). Moreover, in all the investigated mixes, Penetron (Collegno, Torino, Italy) Admix crystalline admixture was used as a stimulator of the autogenous self-healing capacity, dosed at 0.8% by weight of cement (Cuenca et al. 2021b). Its morphological and chemical characteristics were described by Cuenca et al. (2018); it is a powder consisting of portland cement, quartz sand, and other reactive proprietary chemicals. In addition, two further mixes, based on the reference UHDC-CA, were produced: UHDC-CA+ANF, containing 0.25% by weight of cement alumina nanofibers (ANFs); and UHDC-CA+CNC, containing 0.15% by weight of cement cellulose nanocrystals (CNCs).

The interest in including the aforementioned nanoconstituents was explained in detail in the section "Introduction." Alumina nanofibers (Nafen, Tallinn, Estonia) had an average diameter between 4 and 11 nm and a length of 100–900 nm, with a specific surface of 155 m^2/g. To facilitate the mixing process in concretes with low water/binder ratios, this product is supplied in a water suspension with a solid phase concentration equal to 10%. Cellulose nanocrystals (API Europe, Athens, Greece) had an average diameter of 5 nm and were 50–500 nm in length, and were supplied in water suspension at 10% solid content.

Sample Preparation and Curing Conditions

For this investigation, different specimens based on the test requirements were produced: prismatic specimens 40 × 40 × 160 mm for shrinkage, flexural, and compressive strength, self-healing, and water sorptivity tests; and cylinders, Ø100 mm × 300 mm high, from which 50-mm-thick disks were obtained for characterization of microstructure and intrinsic durability parameters, including chloride transport and water capillary suction.

After demolding, all specimens were cured in a moist room [T = 20°C, relative humidity (RH) = 95%] until the related tests were performed. A series of 40 × 40 × 160 mm samples also was cured immersed in geothermal water to analyze the mechanical and durability behavior of sound and cracked concrete exposed to aggressive acid environments (XA exposure conditions). The geothermal water came from the cooling water tanks of a geothermal power plant owned by Enel Green Power (a partner of the ReSHEALience project) in Tuscany (Italy) (Table 2).

Experimental Tests and Methods

The mechanical and durability behavior of concrete exposed to aggressive chemical environments was analyzed in uncracked and cracked states. Tests in the uncracked state (section "Mercury Intrusion Porosimetry" (MIP) to section "Mechanical Properties") were required to characterize the cementitious matrix of the investigated UHDCs from the microstructural and intrinsic durability points of view, whereas tests of cracked samples (sections "Visual Crack Analysis to Quantify Self-Sealing Capacity" and "Sorptivity Tests for Evaluation of Self-Healing Efficiency") were performed to identify the durability enhancement in expected service conditions (Fig. 1).

Mercury Intrusion Porosimetry

The pore-size distribution and pore volume of the concretes were analyzed in accordance with ISO 15901-1 (ISO 2016) using a Micrometrics Autopore IV 9500 porosimeter (Ottawa, Canada). The pore diameter was derived using Washburn's law, $D = (-4\cos\theta)\gamma/P$, where D is the pore diameter (μm), θ is the contact angle between the fluid and the pore mouth (141. 3°), γ is the surface tension of the fluid (485 N/m), and P is the pressure applied to fill the pore with mercury (MPa). The maximum pressure applied was 227 MPa. Samples employed for these tests consisted of pieces of about 1 cm^3 volume, obtained from the Ø100 × 50-mm disks. Before testing, the samples were vacuum dried for 1 week. Tests were performed at 2 and 24 months of age in a moist room.

Microstructural Analyses

Thermogravimetric analysis (TGA) was used to identify phase composition differences and quantitatively determine the bound water, portlandite, and calcite contents in the investigated UHDCs after 2 months. TGA was carried out using an SDT Q600 instrument (TA Instruments, New Castle, Delaware); 40 mg of a powder sample was heated from 25°C to 1,000°C at a heating rate of 10°C/min, under a nitrogen flowing atmosphere. An X-ray diffraction test (XRD) was performed to determine the crystalline phases. Tests were carried

Table 3. Chemical composition of cement (PC) and ground granulated blast-furnace slag (GGBS)

Oxide (% by weight)	CaO	SiO_2	Al_2O_3	MgO	SO_3	Fe_2O_3	TiO_2	Mn_2O_3/MnO	K_2O	Na_2O	Other	LOI
PC	59.7	19.5	4.9	3.3	3.4	3.5	0.2	0.1	0.8	0.2	0.4	2.5
GGBS	39.2	38.9	10.2	6.4	1.3	0.4	0.6	0.3	0.5	0.8	0.3	1.2

Note: LOI = loss on ignition at 1,000°C.

J. Mater. Civ. Eng., 2022, 34(8): 04022154

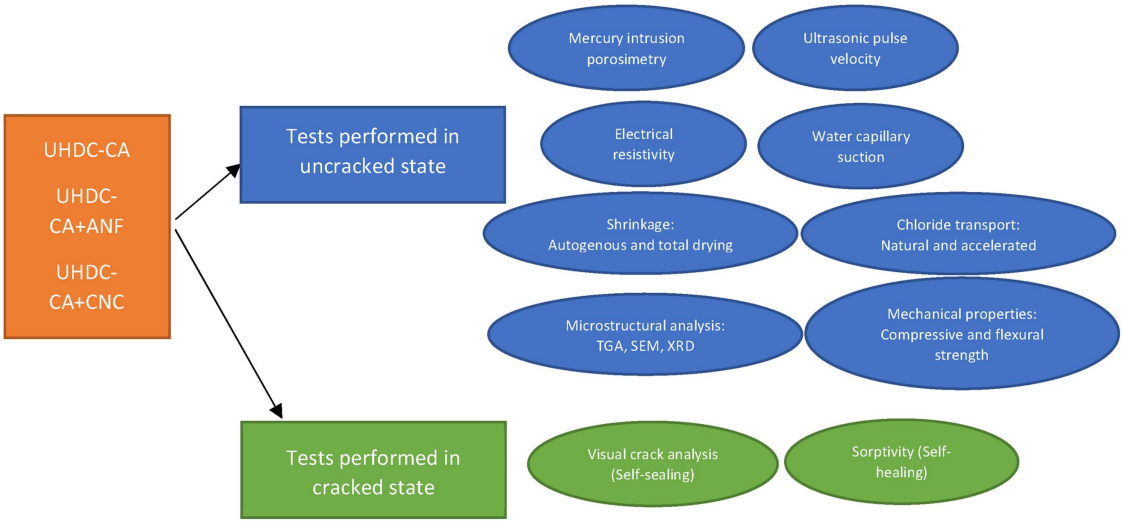

Fig. 1. Flow chart of the research.

out on powdered concrete using a Bruker D8 (Billerica, Massachusetts) Advance instrument with Cu-Kα radiation and a nickel filter. The tests were conducted with a step size of 0.02° and a counting time of 0.5 s/step, from 5° to 60° 2θ. The scanning electron microscopy (SEM) microstructure was investigated using a Hitachi (Chiyoda, Tokyo) S-4800 scanning electron microscope in backscattered mode (BSEM) equipped with a Bruker 5030 energy dispersive analyzer under 20 kV accelerating voltage and a beam current of 20 μA. Pieces of concrete of about 20 mm were embedded into an epoxy resin, cut, polished, and coated with carbon prior to obtaining the images.

Ultrasonic Pulse Velocity

Ultrasonic pulse velocity was determined using standard EN 12504-4 (CEN 2006). The ultrasonic pulse velocity was obtained using a Pundit 7 (CNS Farnell, Cusano Milanino, Milan, Italy) with a nominal frequency of 54 kHz and a precision of 0.1 μs. Tests were performed at 2 and 6 months of age. The dynamic Young's modulus was calculated from the garnered data.

Chloride Transport

Chloride transport was evaluated following two procedures: (1) accelerated chloride transport, based on electrical migration, and (2) natural chloride transport, based on diffusion. In the first method, the chloride transport was determined after 2 months of aging following the recommendations of the NT Build 492 standard (Nordtest 1999). The chloride migration coefficient (D_{nssm}) from non-steady-state migration experiments was determined. During the execution of the tests, the voltage and the time were adapted according to the type of concrete to assure a minimum level of charge pass during the test: 15 V potential difference was applied for 24 h to the UHDC-CA and UHDC-CA+CNC mixes, and 25 V was applied for 24 h to the UHDC-CA+ANF mix. The high content of fibers used in the investigated materials limited the determination of the chloride profile for natural diffusion coefficient estimation. Instead, the NT515 standard (Nordtest 2015) was adapted to study the evolution of chloride penetration depths and the percentage of total and free of chlorides in 1 cm after 6 and 24 months of exposure. The specimens were preconditioned and exposed to a ponding chloride solution (3% NaCl) following the recommendations of CEN 12390-11 (CEN 2019). After 6 and 24 months, the specimens were removed from the chloride source and the chloride penetration depth and the percentage of chlorides in 1-cm depth was determined to evaluate the natural chloride transport. To do this, the specimens were split into two halves, and the penetration depth was determined on one half by applying silver nitrate solution. From the other half, one layer 1 cm from the surface in direct contact with the chloride solution was cut and ground, and the percentages of total and free chloride content were analyzed.

Water Capillary Suction Tests

The water transport resistance was analyzed through capillary suction tests. The test method described in UNE 83982 (UNE 2008a) was followed, which allowed determining the water capillary suction coefficient (k).

Electrical Resistivity

The electrical resistivity test followed the standard UNE 83988-1 (UNE 2008b). The measurements were performed with an Autolab 84750 (Metrohm Autola, Utrecht, Netherlands) potentiostat/galvanostat using the direct method. Measurements of electrical resistivity were made using a pure sine wave AC voltage of 32 mV RMS at a frequency of 10 kHz. Tests were performed on 2- and 6-month-old specimens.

Shrinkage

Shrinkage deformation was measured using a length comparator [(EN 12617-4 (CEN 2002b)] on prismatic specimens cured in a climate room at 20°C and 50% RH. Shrinkage was measured until the values reached a horizontal asymptote. Both total drying and autogenous shrinkage were measured; for autogenous shrinkage, the specimens were sealed with aluminium foils.

Mechanical Properties

Specimens were demolded 1 day after casting and subsequently cured for different periods in either a moist room ($T = 20$°C, RH = 95%) or completely immersed in geothermal water. For both curing conditions, mechanical tests were performed at the age of 28, 56, and 84 days. Flexural and compressive strengths were measured on an Instron 8562 (Norwood, Massachusetts), performed according to standard EN 1015-11-1999 (CEN 2020) on 40 × 40 × 160-mm prisms. An 8-mm-deep notch was cut the midspan of the specimens to localize the crack and facilitate the measurement of crack mouth opening displacement (CMOD), which served as a strain controlling test variable.

Visual Crack Analysis to Quantify Self-Sealing Capacity

Specimens were precracked up to a residual CMOD value of 150 μm at 28 days after casting using a three-point bending test setup. The test was strain controlled at a CMOD rate of 0.5 μm/s. The visual crack analysis was performed on precracked and healed specimens to analyze the crack sealing phenomenon using a digital microscope. To activate self-sealing, specimens were immersed in geothermal water for 1, 3, and 6 months. To measure the crack area, a digital microscope was used with a magnification factor of 45× for bottom surfaces and 205× for side surfaces. To obtain a full representation of each crack, 10–12 pictures from different spots were taken and then collated using image-editing software Photoshop version CS6. The procedure to obtain the crack geometry parameters, either in terms of crack width or crack area, was described in detail by Cuenca et al. (2018). Following this procedure for both newly formed cracks and the same cracks after the sealing period (1, 3, or 6 months), the extent of self-sealing was assessed by calculating the crack sealing as

$$\text{Crack sealing}\,(\%) = \left(\frac{A_{\text{cracked}} - A_{\text{sealed}}}{A_{\text{cracked}}}\right) \cdot 100 \qquad (1)$$

where A_{cracked} = area of crack after precracking; and A_{sealed} = area of crack after sealing period (1, 3, or 6 months).

Sorptivity Tests for Evaluation of Self-Healing Efficiency

The self-healing performance of precracked specimens was determined after 1, 3, and 6 months, during which the specimens were immersed permanently in geothermal water. Sorptivity tests were carried out to determine the sorption coefficient (SC) and assess the healing efficiency (HE). Tests were carried out on prismatic specimens (40 × 40 × 160 mm) based on EN 13057 (CEN 2002a). These tests were performed in three different sample conditions: uncracked, cracked, and healed-crack samples. Before performing the tests (at the end of the scheduled healing period in the intended exposure condition), specimens were dried in an oven at 40°C until a constant weight was achieved, and then kept in a dry room (20°C, 50% RH) for 24 h. A silicon-based waterproofing layer was applied, covering all the surfaces except a 20 × 40-mm area at the specimen center, where a notch previously had been cut to enforce unidirectional water flow during the test (Cuenca et al. 2021c). The sorptivity test was conducted by placing the samples on supports and immersing them in tap water with a constant level of water 3 mm above the notch tip (Cuenca et al. 2021c). The water uptake was calculated as the difference between the weight of the specimen after immersion in water and its initial weight before the sorptivity test. The water uptake was plotted versus the square root of time, and the slope of this curve provided the sorption coefficient. The HE was calculated using the following equation]:

$$\text{HE}(\%) = \frac{\text{SC}_{\text{cracked}} - \text{SC}_{\text{healed}}}{\text{SC}_{\text{cracked}} - \text{SC}_{\text{uncracked}}} \times 100 \qquad (2)$$

Results and Discussion

Physical and Mechanical Properties of UHPFRCs with GGBS and Nanoconstituents

Compressive Strength

Fig. 2 shows, for all the investigated mixes, the compressive strength values at 28, 56, and 84 days, which ranged from 120 to about 180 MPa, as expected for a UHPFRC. The presence of nanoconstituents and the effect of exposure conditions on the compressive strength were not significant, but some improvement was more significant at early ages [Fig. 2(a)], probably as a consequence of enhancing the cement hydration due to the nanoconstituents, as claimed by Cao et al. (2015), Kawashima and Shah (2011), Gopalakrishnan and Jeyalakshmi (2018), Sánchez and Sobolev (2010), and Li et al. (2006) and confirmed in the present work with the microstructural analyses [i.e., thermogravimetry (TG)/differential thermal analysts (DTA)]. The measured limited experimental scattering can be interpreted as an indicator of good fiber dispersion inside the specimens [Fig. 3(a), SF] in addition to the sand [Fig. 3(a), S] particles' homogenous distribution in the cement paste matrix. Furthermore, a dense microstructure [Fig. 3(b)] of the matrix shows the good quality ITZ of the steel fiber and cement paste, indicating a good joint between both concrete components.

Concrete Homogeneity and Density

MIP results for the pore-size distribution are shown in Fig. 4(a) at earlier and long-term curing ages (2 and 24 months). The pore network was distributed mainly on capillary pores less than 0.2 μm.

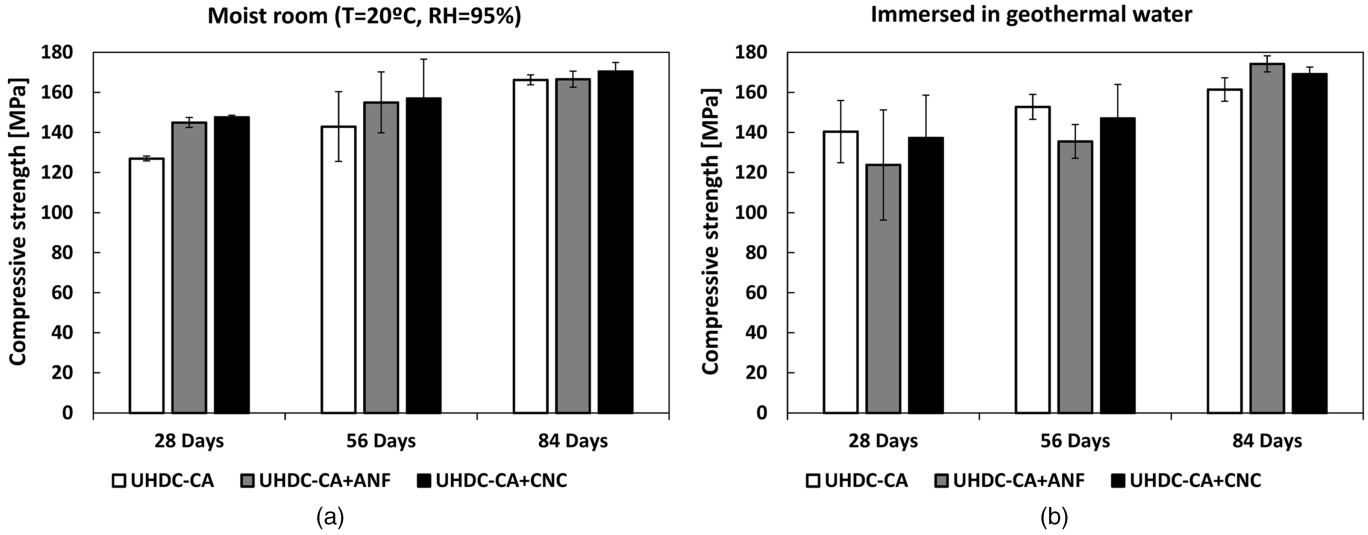

Fig. 2. Compressive strength values of all mixes for specimens: (a) cured in a moist room (T = 20°C, RH = 95%); and (b) immersed in geothermal water.

J. Mater. Civ. Eng., 2022, 34(8): 04022154

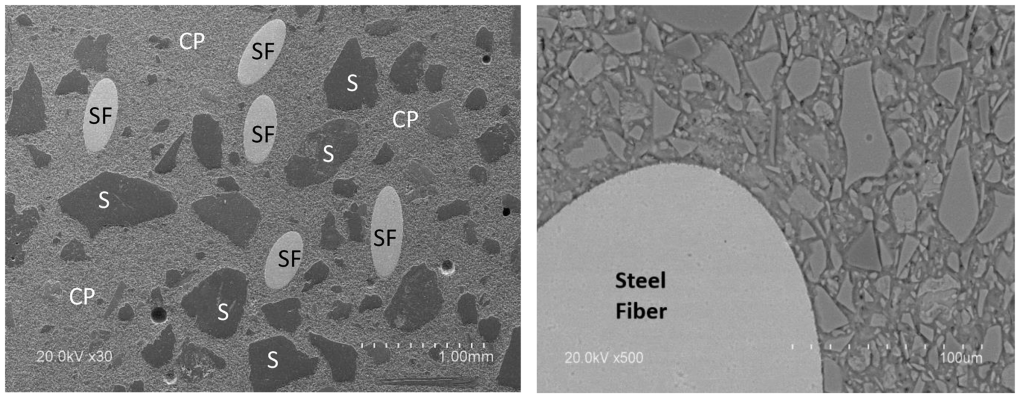

Fig. 3. (a) Microstructure (magnified 30×) of UHDC-CA+ANF showing cement paste (CP), steel fiber (SF), and sand (S); and (b) steel fiber–cement paste interface (magnified 500×).

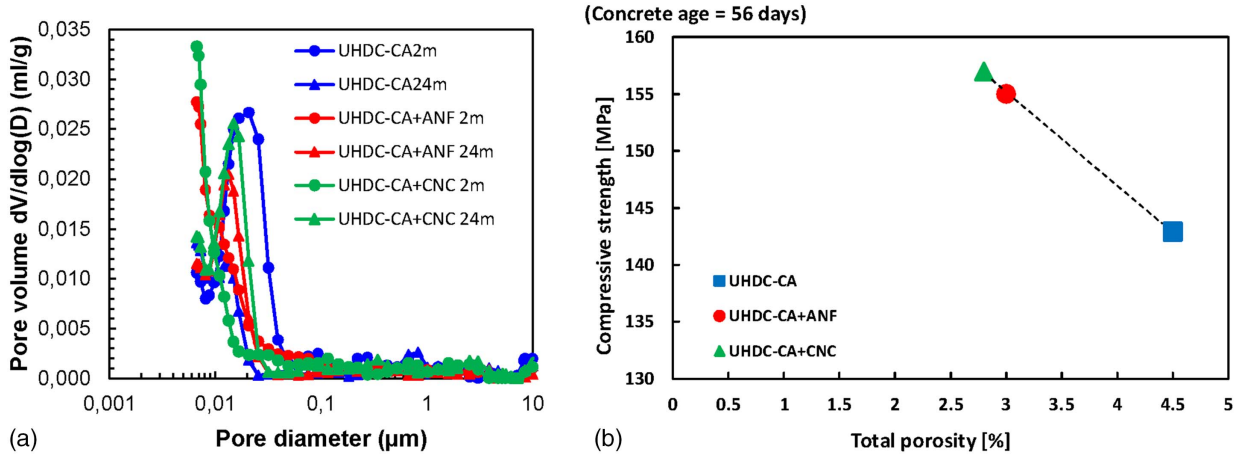

Fig. 4. (a) Differential pore volume for UHDC-CA, UHDC-CA+ANF, and UHDC-CA+CNC concretes at 2 and 24 months; and (b) relationship between total porosity and compressive strength of specimens cured in a moist room for 56 days.

Table 4. Pore structure characteristics of concretes

	UHDC-CA		UHDC-CA+ANF		UHDC-CA+CNC	
Parameter	2 months	24 months	2 months	24 months	2 months	24 months
Total porosity (%)	4.35	2.46	2.98	2.80	2.84	2.86
Apparent density (g/mL)	2.54	2.57	2.48	2.44	2.53	2.58
Average pore diameter (μm)	0.021	0.021	0.017	0.018	0.016	0.020
Tortuosity	22.10	6.34	12.84	1.98	11.43	4.07

The UHDC-CA mix at 2 and 24 months had a main peak pore distribution between 0.1 and 0.01 μm, whereas an evolution to smaller capillary pores (<0.02 μm) was detected in the concretes containing both of the nanoconstituents, UHDC-CA+ANF and UHDC-CA +CNC. The refinement of the pore structure at early ages due to the incorporation of ANF and CNC also contributed to the beneficial effect of these nanoadditives on compressive strength [Fig. 4(b)], based on tests performed at the same age, 56 days, for specimens cured in a moist room.

The concrete pore network characteristics summarized in Table 4 indicate that the total porosity, mean pore diameter, and tortuosity decreased with age and with the incorporation of the nanoconstituents. The total porosity of the three studied mixes was between the limit values of 3% to 5%, and always was less than 3% at greater ages, indicating vthat ery high density contributed to enhancing the durability response, as is expected for a UHDC (Wang et al. 2014; Baroghel-Bouny 2004) and also confirming the pore-refining activity of the CA in the longer term. The contribution of the nanoadditives used in this study can be explained by the enhancement of hydration products, as claimed by Gopalakrishnan and Jeyalakshmi (2018) and also demonstrated in the present paper from TG/DTA data presented subsequently. Moreover, the alumina nanofibers also can act as filler, densifying the microstructure and leading to reduced porosity and average pore diameter (Sánchez and Sobolev 2010; Li et al. 2006). In the case of the nanocellulose, its ability to retain water that can be released subsequently similar to the internal curing phenomenon in the matrix. That results in generation of larger hydration products that precipitate inside the small pores

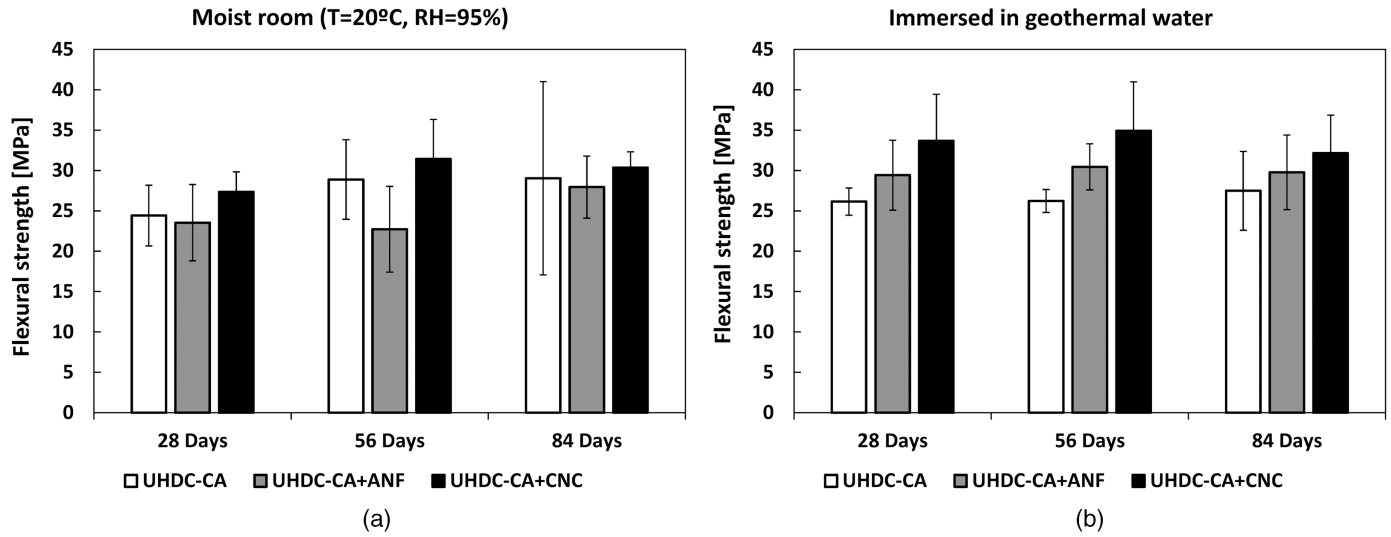

Fig. 5. Flexural strength values of all mixes for specimens: (a) cured in a moist room ($T = 20$°C, RH $= 95\%$); and (b) immersed in geothermal water.

of the matrix, which explains the refinement of pore structure with the maturity of the concrete from 2 to 24 months. This phenomenon reduces the porosity and tortuosity, and hence increases the matrix densification (Kawashima and Shah 2011; Claramunt et al. 2019).

Flexural Strength

The average flexural strengths of all mixes cured in both conditions (moist room and immersion in geothermal water) are presented in Fig. 5.

The high values of flexural strength were due mainly to the quite significant amount of steel fibers (120 kg/m^3) incorporated into all the mixes. Moreover, the incorporation of nanoconstituents did not result in increased flexural strength for specimens cured in a moist room [Fig. 5(a)]; only a very slight improvement was measured when CNC was present (UHDC-CA+CNC mix). On the other hand, when specimens were cured in geothermal water [Fig. 5(b)] a clear increase of the flexural strength was measured due to the presence of nanoconstituents compared to the reference mix, especially for the case of UHDC-CA+CNC. In this case, at 28 days the flexural strength increased 29% compared with that of the reference mix. The increase in flexural strength was confirmed systematically also at later ages: e.g., at the age of 84 days, a 27% increase for UHDC-CA+CNC compared with UHDC-CA was observed. These findings are in accordance with those of previous studies, e.g., Cao et al. (2015), who measured a 30% increase in the flexural strength using 0.2% volume of CNC with respect to cement, and attributed it to an increase in the degree of hydration of the cement paste. It is likely that the CNC improves material performance, also through densification of the fiber–matrix interface, providing their best effects when the material is exposed to an aggressive environment. However, a clear explanation of this performance does not exist in such aggressive media for conventional concretes, and the mixes herein investigated were all of the UHPC type.

Elastic Properties

The results of ultrasonic pulse velocity (UPV) tests for the UHDC-CA, UHDC-CA+ANF, and UHDC-CA+CNC after 2 and 6 months of curing are reported in Fig. 6(a). The UPV values were between 4.6×10^3 and 4.8×10^3 m/s, corresponding to a very dense and high-quality concrete (Zhang et al. 2012). The incorporation of nanoconstituents resulted in negligible differences that can be explained by the sensitivity of the technique to the very dense matrixes or by the presence of fibers, through which p-waves move forward faster than through cement, aggregates, or nano-additions (about 5×10^3 m/s). The evolution of the elastic properties is indicated by the slight increase of values from 2 to 6 months.

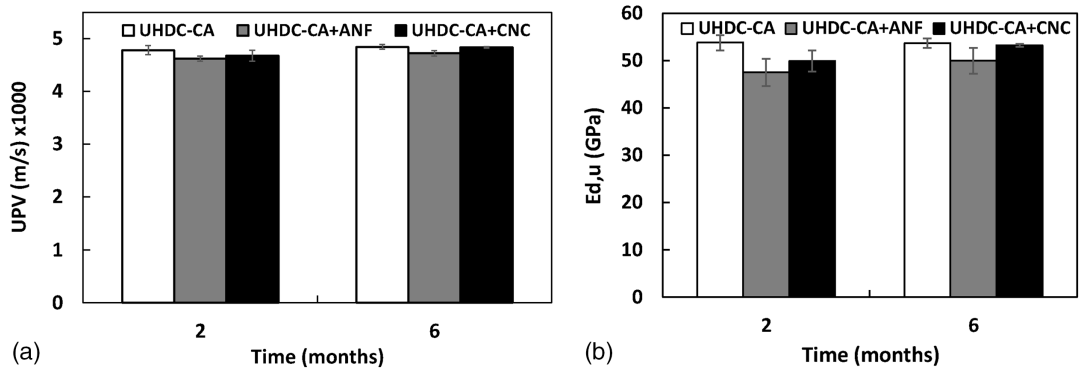

Fig. 6. UHDC-CA, UHDC-CA+ANF, and UHDC-CA+CNC at 2 and 6 months of curing: (a) UPV values; and (b) dynamic elastic modulus ($E_{d,u}$) values.

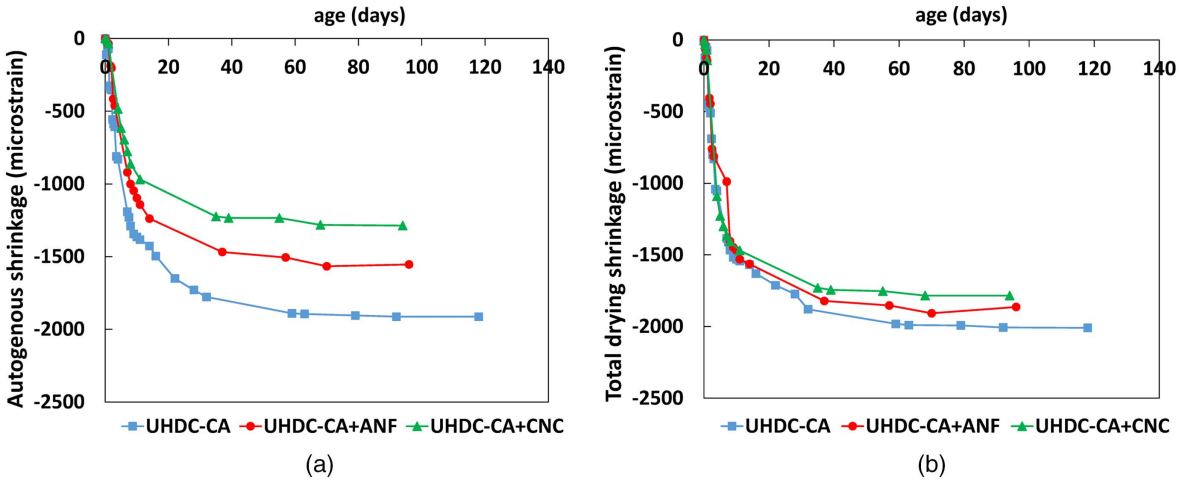

Fig. 7. (a) Autogenous shrinkage; and (b) total drying shrinkage.

Under the assumption that UHDC, as enhanced UHPFRC with nanoconstituents, can be considered a homogeneous isotropic elastic medium (Hassan and Jones 2012), the dynamic elastic modulus ($E_{d,u}$) can be calculated as follows:

$$V_{p,s} = \sqrt{\frac{E_{d,u}}{\rho} \cdot \frac{(1-\nu)}{(1+\nu)\cdot(1-2\nu)}} \tag{3}$$

where $V_{p,s}$ = compression wave velocity; ρ = density of concrete; and ν = Poisson's ratio, which can be considered to be 0.2 in concrete and UHPFRC (Hassan and Jones 2012). The values of $E_{d,u}$ [Fig. 6(b)] indicate the high elastic modulus expected for a UHPFRC, ranging from 47.8–52.3 GPa at 2 months to 49.9–53.7 GPa at 6 months, with a small scatter in the measurements.

Shrinkage

Autogenous and total drying shrinkage are shown in Figs. 7(a and b), respectively, for all the investigated mixes, characterized by a high amount of cement and slag and low water/cement ratios, which resulted in higher shrinkage, mostly of the autogenous type, although a similar trend was observed for the total drying shrinkage [Fig. 7(b)].

The presence of nanoconstituents resulted in a reduction of shrinkage deformation of concrete with respect to the concrete age. A 32% decrease in the autogenous shrinkage of UHDC-CA+CNC compared with that of the reference mix UHDC-CA was observed at 100 days, and the values remained quite stable beyond this age. For total drying shrinkage, CNCs acted as moisture exchange pathways, due to their hydrophilic nature, and thus did not produce any significant reduction in the total shrinkage deformation. The presence of nanoconstituents mainly reduced the autogenous shrinkage (in particular, the nanocellulose is very effective promoting the internal curing inside the matrix) more than the total drying shrinkage, which also was in accordance with the literature (Hisseine et al. 2020; Lee et al. 2019). Moreover, it was supported by the mass loss measurements of the same specimens employed for total drying shrinkage measurement, which showed that the reference mix without nanoconstituents (UHDC-CA) had the lowest mass loss [Fig. 8(a)]. The reduction in porosity due to the presence of nanoconstituents also can contribute to the reduction in shrinkage deformation, as confirmed by the relationship between total porosity (%) and shrinkage (autogenous and drying) measured at the same age (56 days) [Fig. 8(b)]. The positive effect of internal curing and nanolevel reinforcement also was confirmed by

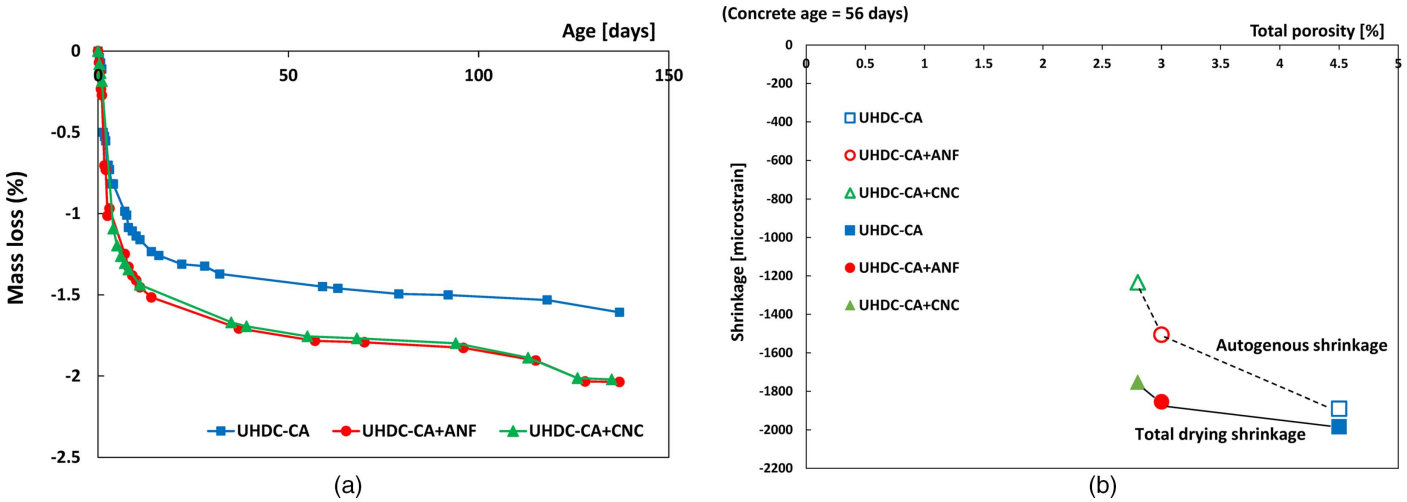

Fig. 8. (a) Mass loss; and (b) influence of the total porosity on the shrinkage deformation.

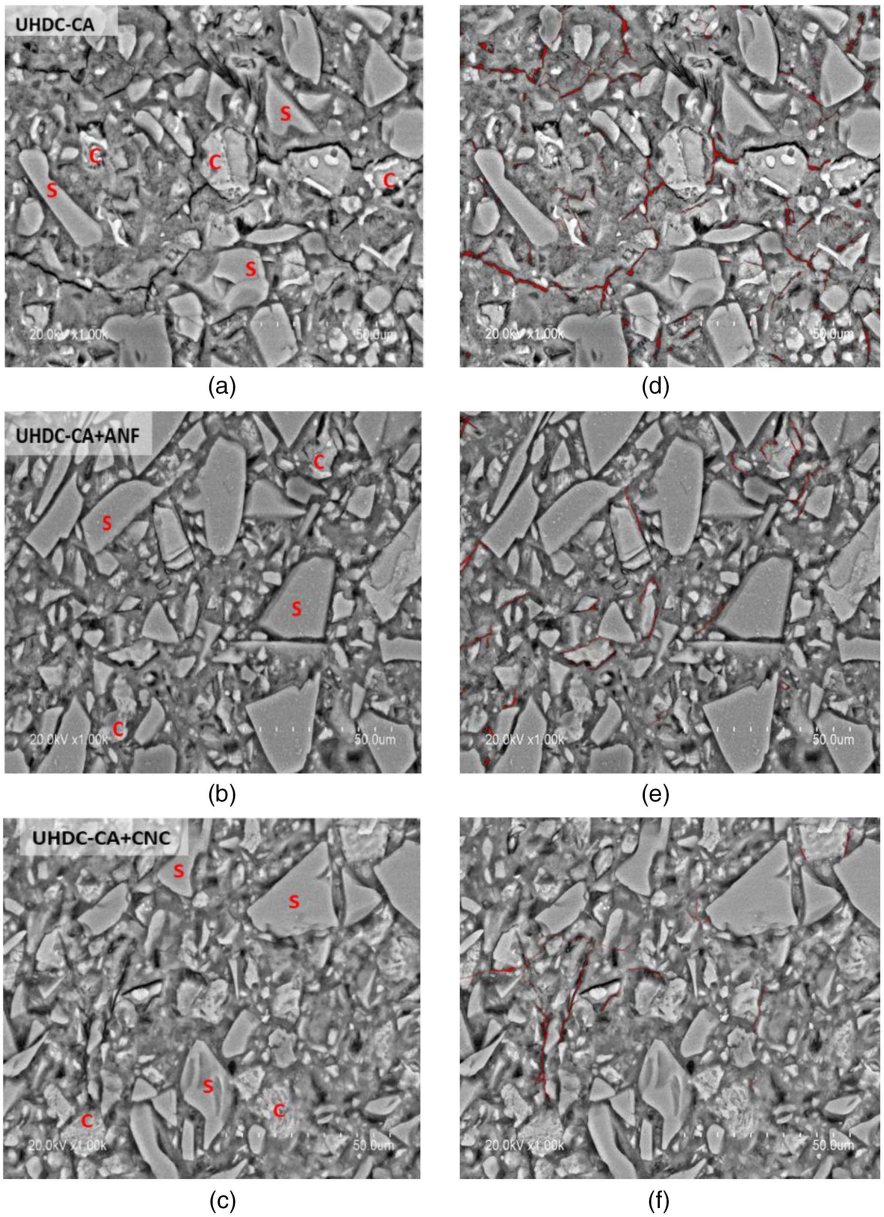

Fig. 9. (a) Microstructure (magnified 1,000×) of UHDC-CA showing microcracking in cement paste; (b) UHDC-CA+ANF showing denser microstructure (magnified 1,000×) with much less severe microcracking; (c) UHDC-CA+CNC showing denser microstructure (magnified 1,000×) with much less severe microcracking; (d) microstructure (magnified 1,000×) of UHDC-CA showing microcracking in cement paste, with patterns indicating the presence of microcracks highlighted; (e) microstructure (magnified 1,000×) of UHDC-CA+ANF showing microcracking in cement paste, with patterns indicating the presence of microcracks highlighted; and (f) microstructure (magnified 1,000×) of UHDC-CA+CNC showing microcracking in cement paste, with patterns indicating the presence of microcracks highlighted.

Barnat-Hunek et al. (2019) and Hisseine et al. (2020) and by a deep microstructural characterization carried out using BSEM of the UHDC-CA, UHDC-CA+ANF, and UHDC-CA+CNC mixes [Figs. 9(a–c)]. The presence of microcracks was highlighted in each micrograph by means of GIMP 2.10.4 software [Figs. 9(d–f)]. Small microcracks were observed in the cement paste with only the CA, whereas there are far fewer microcracks with the incorporation of ANF or CNC due to the aforementioned effects. Homogeneity of microcracks was detected throughout the entire UHDC-CA sample. These results further corroborate the assumptions about the mechanisms responsible for shrinkage reduction in the presence of nanoadditions.

SEM images also provided an overview of the dense microstructure of the three studied UHDCs after 60 days of aging in a moist room (Fig. 9). The large angular light grey particles corresponding to unreacted slag grains (Fig. 9, S), and the unreacted (or partially reacted) cement particles (Fig. 9, C) all were surrounded by a dense and compact matrix (medium grey area) corresponding to the main binding phases. These phases exhibited surface continuity, with low porosity, which, also is the reason of the high compressive strength of the investigated cementitious composites. The number of anhydrous cement and GGBS grains still was very significant. Further investigation of the microstructure is provided in the following section.

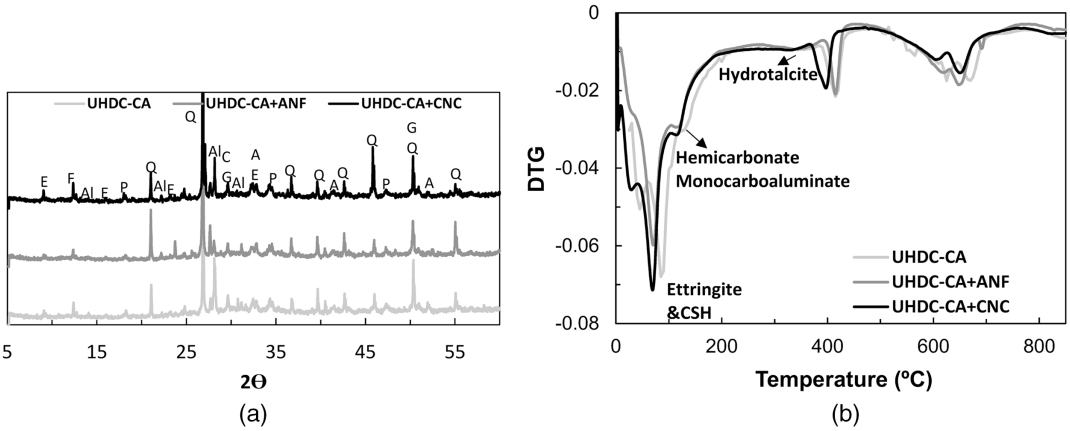

Fig. 10. (a) XRD of the investigated UHDC mixes (Q = quartz, E = ettringite, P = portlandite, C = calcite, Al = albite, A = alite, G = C—S—H, and F = ferrite); and (b) DTG curves of the UHDC-CA, UHDC-CA+ANF, and UHDC-CA+CNC concretes at 60 days.

Characteristics of Cement Paste in UHDC with GGBS and Nanoconstituents

The X-ray diffraction patterns of the UHDC-CA, UHDC-CA +ANF, and UHDC-CA+CNC after 2 months of curing are reported in Fig. 10(a). Similar crystalline phases were detected in the three UHDCs which were typical of hydrated cement paste, including calcium silicate hydrate. The presence of portlandite also was indicated, but only residual ettringite, although monocarboaluminate, hemicarbonate or hydrotalcite cannot be disregarded. As suggested by Fernández et al. (2018) in cement pastes with 30% GGBS content, or higher, all these hydrated phases will contribute later to interact with aggressive water ions as chloride or sulfates. The peak of diffraction associated with C—S—H (29.5°Θ) overlaps with the most intense peak of the calcite. The diffractograms also indicate the presence of quartz and albite, which were associated with the aggregate and slag, as well as a significant content of unreacted cement particles as alite and ferrite phases. The presence of the nanoconstituents (alumina nanofibers or cellulose nanocrystals) did not affect the stability of the hydrated phases because analogous phases were detected in the related diffractograms, compared with those recorded for the UHDC-CA concrete. The diffraction peak at 18.0°Θ appears in all concretes and is associated with portlandite and related to the progression of cement hydration. The peak at 29.5°Θ is related to the calcite phase, partly as a consequence of CA addition, also identified by Ferrara et al. (2014). Thermogravimetric analysis of the three concretes, Fig. 10(b), shows the derivate weight loss that allows identifying the temperature stability of hydrated cement paste phases. A mass loss in the 110°C–170°C region is more evident for the ANF and CNC mixes, likely as a consequence of stimulation of hydration induced by the nanoconstituents. This peak is associated with the dehydration of the hemi- or monocarboaluminate, as suggested by Fernández et al. (2018), and also can be related to a certain reaction between the calcium carbonate, the production of which also may be stimulated by the CA, and the aluminate hydrates of the binder. Monocarboaluminate causes the stabilization of ettringite, thus increasing the volume of hydration products, which can improve the compressive strength measured in the concretes with ANF and CNC. A shoulder appears just before the portlandite peak that can be attributed to hydrotalcite and which also increases in intensity with BFS hydration (Fernández et al. 2018). Three main peaks are common in portland base concretes: (1) a peak up to 350°C is associated mainly with C—S—H gel dehydration, but also with other aluminate phases (Kumar et al. 2008; Soin et al. 2013), (2) a peak at 400°C–500°C is associated with portlandite dehydration (Kumar et al. 2008; Soin et al. 2013), and (3) a peak at 650°C–750°C is associated with the decomposition of carbonates (Kumar et al. 2008; Soin et al. 2013).

The mass loss by weight of cement was estimated at different temperature ranges for bound water, portlandite, and calcite (Table 5). The bound water contents were quite similar for the three cementitious composites, and ranged between 2.13 and 2.25. Some higher portlandite content in the concretes with alumina nanofibers or cellulose nanocrystals was a consequence of higher production of hydration products, probably due to two reasons: the nanoparticles acted as nucleation sites and, in the case of CNC, their ability to cumulate water can favor the hydration of the cement, and in consequence, it can cause the increase of compressive strength, the lower porosity and the lower shrinkage observed in this concrete (Kawashima and Shah 2011).

The chemical composition of the cement paste also was studied by scanning electron microscopy (SEM)/energy dispersive X-Ray spectroscopy (EDX). The main element distribution in cement paste is highlighted in Fig. 11 and expressed as a percentage of the main oxides in Fig. 12 for the three UHDC concretes. Intensive Ca content is indicated. In addition, Al was detected which was distributed homogenously in the cement paste. This also occurred in the case of sulfates or sulfoaluminate phases, detected from XRD and thermogravimetry (TG)/derivative thermogravimetry (DTG) as characteristic due to the presence of GGBS. Anhydrous grains of cement and GGBS were observed clearly. The most characteristic aspect was the high content of CaO, which likely was related to the composition of the type of cement used (Table 3) and the incorporation of the CA.

The percentage distribution of the different oxides in the cement paste shows that the concretes with the CA and ANF and the CA and CNC had a higher CaO content, 60%, than that observed in UHDC-CA (50%). This can be due to the presence of the nanoadditions of ANF and CNC, which stimulated the hydration and

Table 5. Bound water, portlandite, and calcite contents determined by TGA for all studied concretes (% by weight cement)

Concrete	Bound water (100°C–375°C)	Portlandite (375°C–500°C)	Calcite (500°C–750°C)
UHDC-CA	2.25	1.20	3.15
UHDC-CA+ANF	2.13	1.90	2.82
UHDC-CA+CNC	2.25	1.97	2.53

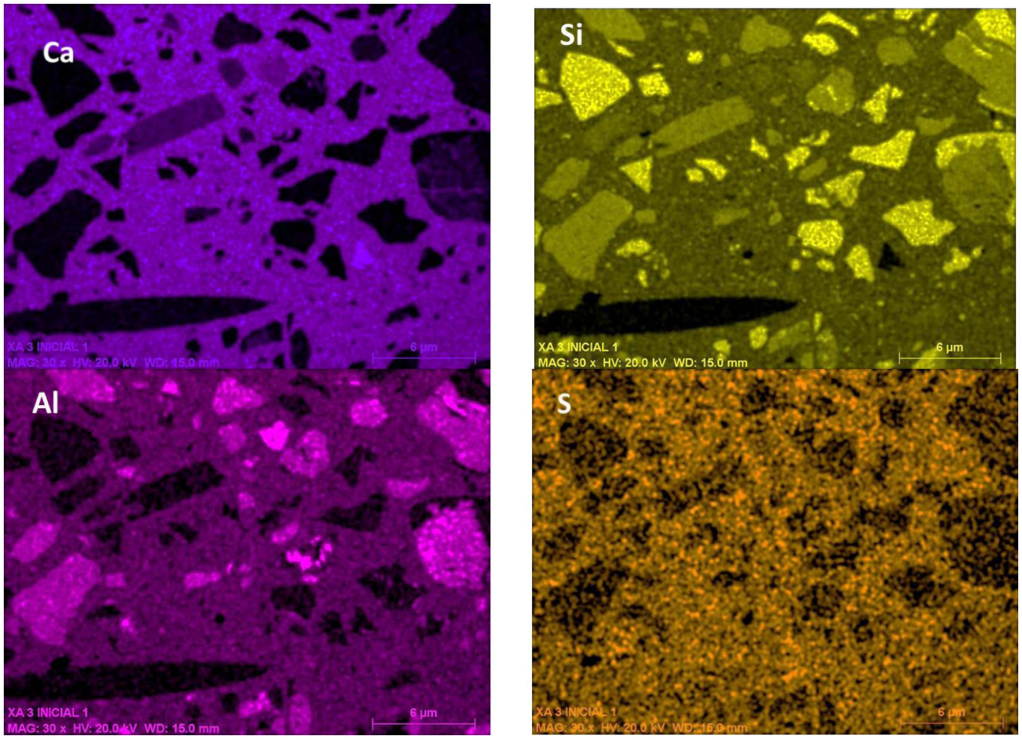

Fig. 11. BSEM mapping (magnified 30×) distribution of main components (Ca, Si, Al, and S) in UHDC-CA.

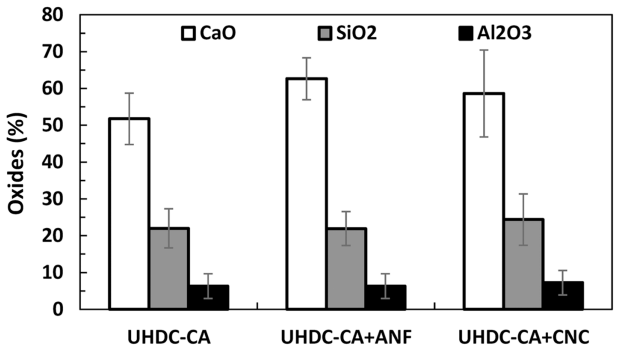

Fig. 12. Main oxide (CaO, SiO_2, and Al_2O_3) distribution percentages of the three concretes.

growth of C—S—H and the formation of hemicarbonate or monocarboaluminate phases detected in the DTG curves. In these two concretes, a greater percentage of portlandite also was formed. In addition, there was hardly any variation of the other main two oxides in cement paste in the three UHDCs studied; the SiO_2 content was 25% and the Al_2O_3 content was 6%–7%. This is $CaO/SiO_2 > 1.8$, which is common in ordinary portland cement paste and higher than that found by Fernández et al. (2018) in a paste also containing 30% GGBS. T Al was detected in the cement paste.

Intrinsic Durability of UHDC with GGBS and Nanoconstituents

To investigate accelerated chloride transport, Fig. 13(a) shows the non-steady-state chloride migration coefficient, D_{nssm} after 2 months of curing. The UHDC-CA concrete had D_{nssm} values of about 0.99×10^{-12} m^2/s. The incorporation of alumina nanofibers and cellulose nanocrystals slightly modified the chloride resistance of concrete, because values of the same order were obtained. However, all these D_{nssm} values, indicating a low permeability of chloride ions for all the investigated mixes, correspond to expected very high durability according to the classification given by Baroghel-Bouny (2004). This good resistance to the accelerated Cl transport in these concretes mainly is a consequence of the low porosity and the compact and dense microstructure of the three investigated concretes.

The natural chloride transport is represented in Fig. 13(b), taking into account the chloride penetration depth and percentage of total and bound chloride (by weight of binder) in 1 cm for the three concretes after 6 and 24 months of the exposure. At low exposure ages (6 months) no significant differences in chloride penetration were observed, mainly due to the low porosity of the concretes, although some penetration values were lower in UHDC containing ANF or CNC. The difference in total Cl penetrated was more evident at longer exposure ages (24 months). The bound chlorides were lower with ANF and CNC, in agreement with some higher cement hydration identified by XRD and TG. In the three concretes, the percentage of bound chlorides was very high (between 40% and 50%), which can contribute to retard the aggressive ion transport, and highlights the beneficial contribution of GGBS. These concretes contained 500 kg/m^3 of blast furnace slag in their formulations, and the presence of this raw material favored the formation of hydrotalcite with excellent efficiency in binding chloride ions and monocarboaluminates, phases which were detected by XRD [Fig. 10(b)], which also adsorb a large amount of chloride ions. These results corroborate those obtained in previous studies, such as those carried out by Kayali et al. (2012), Luna et al. (2018), and Chen et al. (2020), which found an increase in the content of Friedel's salts and the formation of hydrotalcite, enhancing the total capacity of chloride binding of the blended slag cementitious matrixes and retardation of chloride transport.

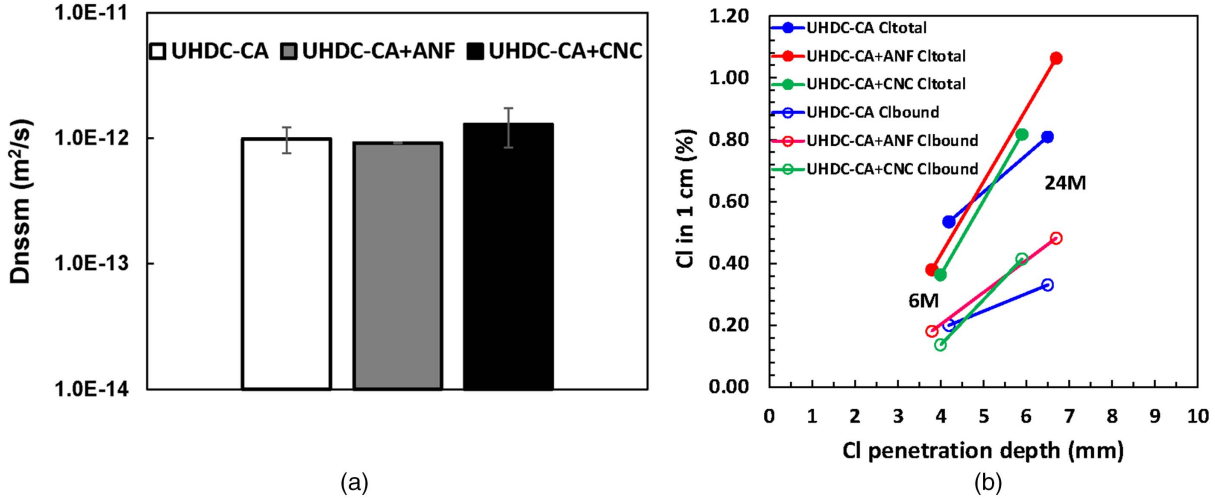

Fig. 13. (a) Chloride migration coefficients (D_{nssm}) from non-steady-state; and (b) Cl penetration depth and percentage of total and bound Cl at 6 and 24 months exposure, indicating natural Cl transport.

These data obtained from the accelerated and natural tests confirm the impermeability of these UHDCs to the penetration of aggressive substances such as chlorides; the incorporation of nanoalumina or nanocellulose led to some improvement, and no negative response was observed, indicating an overall high durability as a consequence of the refined pore network and high Cl binding ability.

Water transport was analyzed through the capillary suction coefficient (k). The water mass gained per unit surface is shown in Fig. 14. Similar water uptake was detected at early exposure time for all concretes with both types of nanoconstituents; the incorporation of neither alumina nanofibers nor nanocellulose crystals resulted in significant changes. Upon longer exposure times after reaching equilibrium, some higher water absorption was measured in the case of the cellulose nanocrystal addition mix, which is likely to confirm that CNC seems to absorb more water in the long term. The capillary suction coefficients showed the clear similarities between the concretes [Fig. 14(b)], with a slight reduction in the case of UHDC with nanoconstituents CNC and ANF, which most likely was correlated with the refined porosity, as was discussed with reference to Fig. 4. Electrical resistivity (ρ_e) also was evaluated (Fig. 15). The UHDC-CA, UHDC-CA+ANF, and UHDC-CA+CNC mixes had resistivity values in the range 20–30 Ωm at 2 months.

After 6 months of curing, an increase of the electrical resistivity occurred, which was related to the progress of hydration, with values ranging between 65 and 140 Ωm. Although limiting values of electrical resistivity between 50–100 and 100–250 Ωm indicate low and average durability, respectively (Wang et al. 2014), the obtained results should not be misleading about the actual level of durability of the investigated mixes with respect to the electrical parameter and compared with the total porosity (Fig. 4) and chloride transport properties (Fig. 13). A reasonable explanation may be the incorporation of steel fibers into the concrete. In addition, a small difference was observed at 6 months, where the concrete containing only the crystalline additive (UHDC-CA) had slightly lower resistivity, while the combination with alumina nanofibers and nanocellulose increased this electrical resistance, the refinement

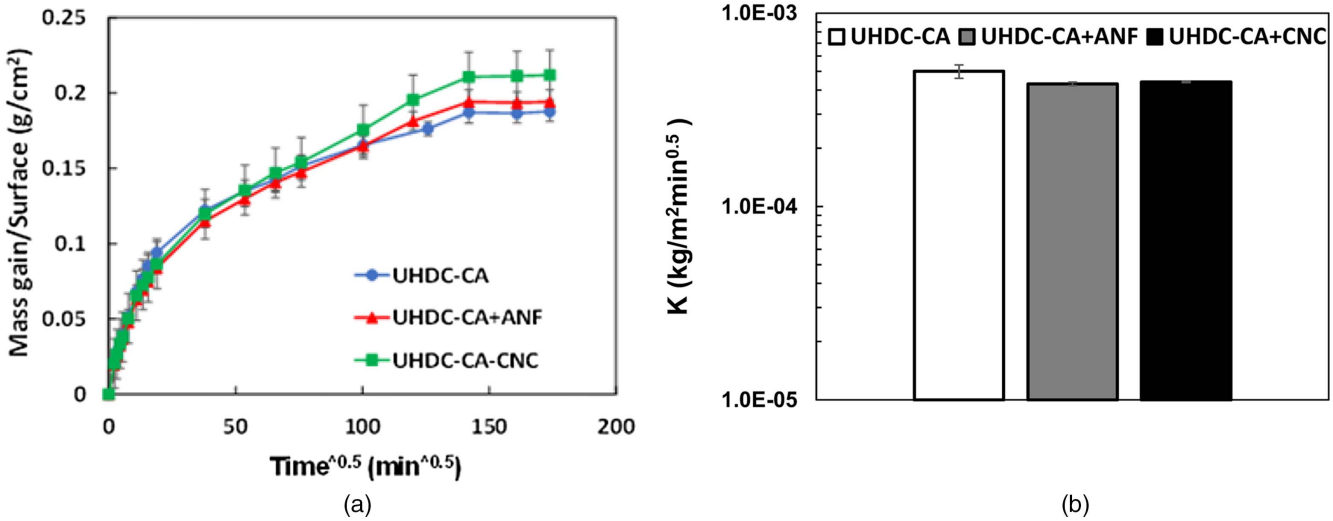

Fig. 14. Water capillary suction coefficient (k) of UHDC-CA, UHDC-CA+ANF, and UHDC-CA+CNC concretes.

of pore structure at long hydration ages, shown in Fig. 4 can explain these results and the beneficial contribution of the nanoadditives that also contribute to reducing the microcracks, as shown in Fig. 9.

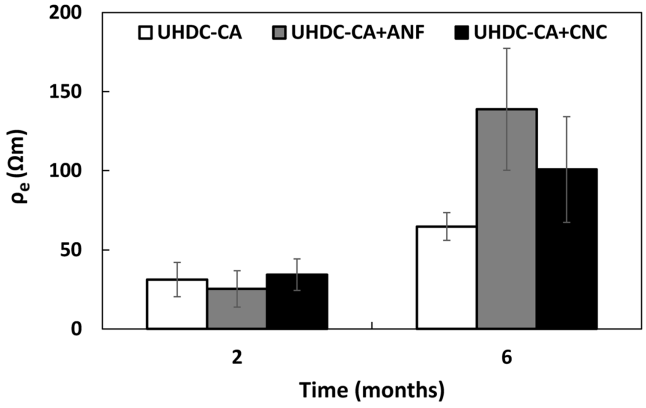

Fig. 15. Electrical resistivity values for the UHDC-CA, UHDC-CA +ANF, and UHDC-CA+CNC concretes at 2 and 6 months of curing.

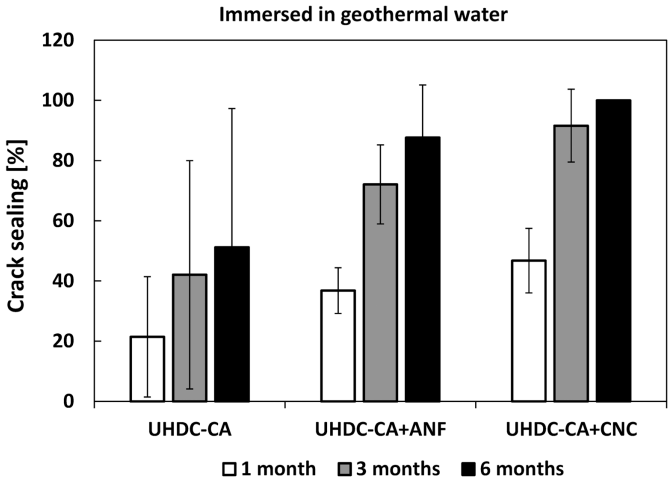

Fig. 16. Crack sealing for specimens immersed in geothermal water for 1, 3, and 6 months.

Enhancing Durability of UHDCs in Cracked State: Self-Healing Capacity

Evaluation of Self-Sealing Capacity of UHDCs: Visual Crack Analysis

Fig. 16 shows the crack sealing percentage for all investigated mixes and healing periods. Crack sealing percentage increased with the presence of nanoconstituents for all studied healing periods.

For a healing period of 1 month, the crack sealing percentage of UHDC-CA+ANF increased by 15.4% and that of UHDC-CA +CNC increased by 25.3% compared with that of the reference mix, UHDC-CA. For a healing period of 3 months, the crack sealing percentage of UHDC-CA+ANF increased by 30% and that of UHDC-CA+CNC increased by 49.5% compared with that of the reference mix, UHDC-CA. After a healing period of 6 months, the crack sealing percentage of UHDC-CA+ANF was 36.49% higher than that of the reference mix, whereas the crack sealing percentage of UHDC-CA+CNC was 48.83% higher than that of the reference mix. Moreover, these values show that the benefits of nanoconstituents improved with longer healing periods (Fig. 16). The stimulating effects of nanoconstituents on cement hydration reactions, discussed previously, reasonably explain this evidence as well.

Evaluation of Self-Healing Capacity of UHDCs: Sorptivity Tests

As expected, the presence of a crack increased the capillary suction (Fig. 17), according to the results of sorptivity tests on uncracked and cracked specimens.

Water uptake curves moved from the cracked to the uncracked state due to self-healing. The better the healing, the lower was the water uptake and, the longer the healing period, the greater was the healing efficiency. Moreover, an increase of the water uptake by capillarity in cracked concretes was detected, which was greater in terms of percentagein the reference mix (UHDC-CA) than in those with nanoconstituents (UHDC-CA+ANF and UHDC-CA +CNC). For the same value of crack mouth opening displacement, the presence of nanoconstituents affect the local opening, tortuosity, and three-dimensional (3D) structure of the crack, generating benefits in this sense. The positive effect of crack healing is shown in Fig. 18(a) in terms of the healing efficiency percentage. After 1 month of healing a 29.9% improvement was measured in the reference UHDC-CA, whereas the effect increased to 35.6% in the mix with UHDC-CA+ANF and to 45% in the mix with cellulose nanocrystals UHDC-CA+CNC. After 3 months of healing a 55.5% improvement was measured in the reference UHDC-CA,

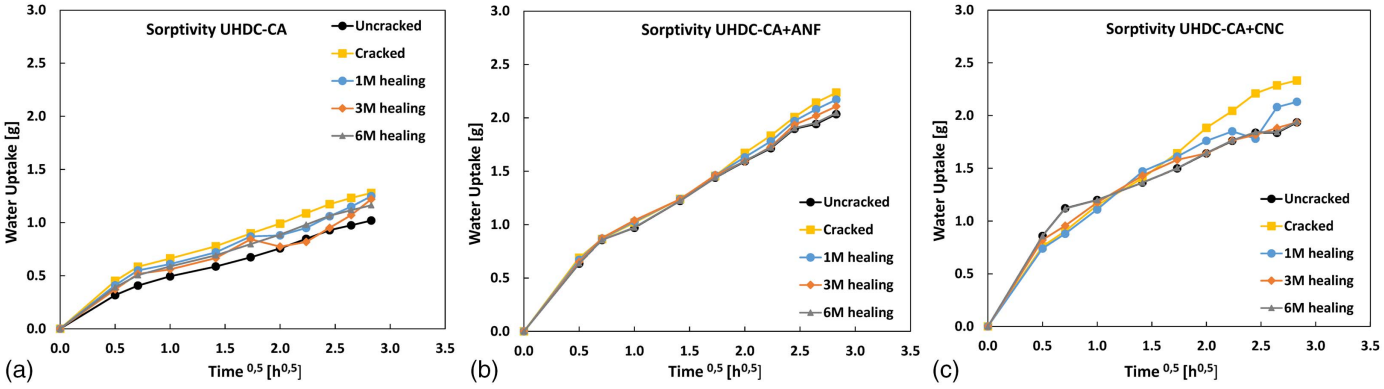

Fig. 17. Water uptake (g) versus time $(h)^{0.5}$ curve for the uncracked-, cracked-, and healed-phase concretes immersed in geothermal water for 1, 3, and 6 months: (a) UHDC-CA; (b) UHDC-CA+ANF; and (c) and UHDC-CA+CNC.

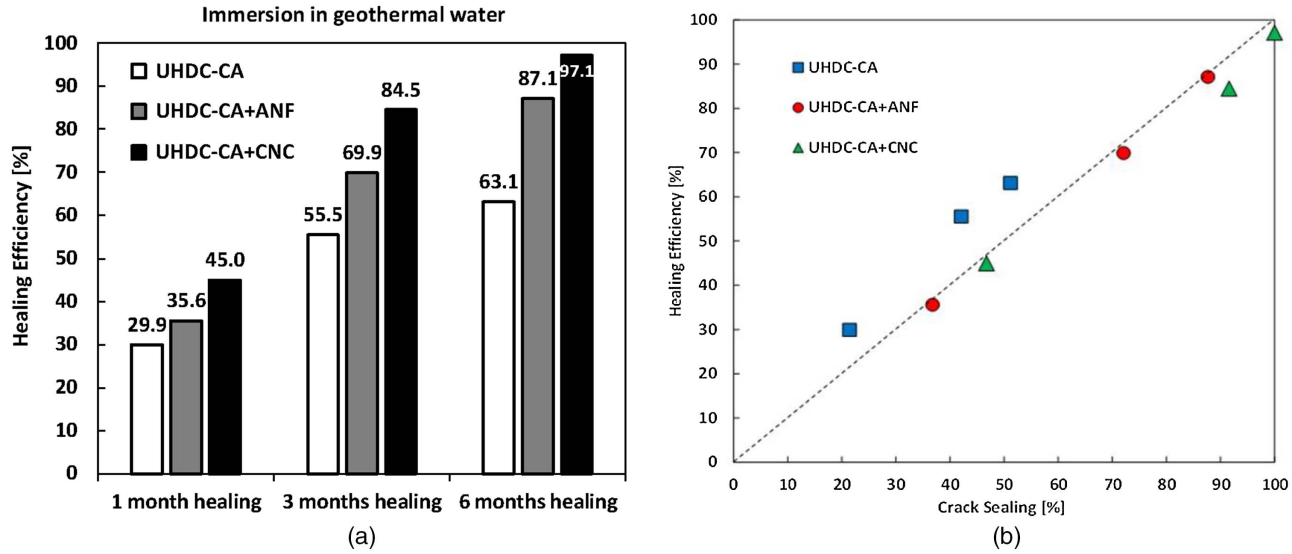

Fig. 18. Healing efficiency of uncracked and healed specimens UHDC-CA, UHDC-CA+ANF, and UHDC-CA+CNC immersed in geothermal water for 1, 3, and 6 months: (a) healing efficiency (%); and (b) healing efficiency (%) versus crack sealing (%).

whereas the effect increased to 69.9% in the mix with UHDC-CA +ANF and to 84.5% in the mix with cellulose nanocrystals UHDC-CA+CNC. Finally, after 6 months, thehealing efficiency was 63.1% in UHDC-CA, 87.1% in UHDC-CA+ANF, and 97.1% in UHDC-CA+CNC. These values highlight the role of nanoconstituents in promoting, through their water uptake, retention, and release capacity, more-effective self-healing of the cracks through delayed hydration reactions.

The healing efficiency calculated from sorptivity tests and crack sealing percentage observed from visual crack analysis for specimens healed immersed in geothermal water have been correlated in Fig. 18(b). The healing efficiency percentage and the crack sealing percentage were strongly correlated in all three investigated mixes. The mixes with nanoconstituents had higher values of both crack sealing percentage and healing efficiency percentage. This trend confirmed the observations throughout this research that nanoconstituents

Table 6. Cumulative results of all UHPFRC mixes before healing

Property	Time	UHDC-CA		UHDC-CA+ANF		UHDC-CA+CNC		Performance improvement with nanoadditives (%)	
		Mean	SD	Mean	SD	Mean	SD	ANF	CNC
Total porosity (%)	2 months	4.35	—	2.98	—	2.84	—	31	35
	24 months	2.46	—	2.80	—	2.86	—	—	—
Portlandite (%)	2 months	1.20	—	1.90	—	1.97	—	58	64
Compressive strength (MPa)									
Developed in moist room	28 days	126.9	1.22	144.9	2.54	147.6	2.57	14	16
	56 days	142.9	17.45	155	4.38	157	15.19	8	10
	84 days	166.3	2.46	166.5	6.61	170.5	4.01	[a]	3
Immersed in geothermal water	28 days	140.4	15.54	123.8	4.14	137.3	27.50	—	[a]
	56 days	152.8	6.23	135.5	3.51	147	8.42	—	[a]
	84 days	161.4	5.84	174.2	2.26	169.2	4.01	8	5
Flexural strength									
Developed in moist room (MPa)	28 days	24.4	3.76	23.5	4.73	27.3	2.49	[a]	12
	56 days	28.9	4.94	22.7	5.31	21.4	4.91	—	—
	84 days	29.0	11.98	27.9	3.84	30.4	1.97	[a]	5
Developed in geothermal water (MPa)	28 days	26.1	1.69	29.4	4.34	33.7	5.78	13	29
	56 days	26.2	1.41	30.4	2.86	34.9	6.08	16	33
	84 days	27.5	4.89	29.8	4.62	32.1	4.71	8	17
Dynamic elastic modulus (GPa)	2 months	52.3	1.6	47.8	2.9	49.8	2.2	[a]	[a]
	6 months	53.71	0.97	49.9	2.7	53.26	0.30	[a]	[a]
Electrical resistivity (Ωm)	2 months	31	11	25	12	34.3	9.9	—	11
	6 months	64.8	8.8	139	39	101	34	114	56
Chloride migration coefficient (m^2/s)	2 months	10×10^{-13}	2×10^{-13}	9.2×10^{-13}	1×10^{-14}	13×10^{-13}	4.5×10^{-13}	7	—
Water capillary suction ($kg/m^2\ mln^{0.5}$)	2 months	50×10^{-5}	4×10^{-5}	43×10^{-5}	9×10^{-6}	44×10^{-5}	3×10^{-6}	14	12

Note: SD = standard deviation; and — indicates no improvement.
[a]Values are quite similar to reference value.

Table 7. Cumulative results of all UHPFRC mixes after healing

Property	Time	UHDC-CA		UHDC-CA+ANF		UHDC-CA+CNC		Performance improvement with nanoadditives (%)	
		Mean	SD	Mean	SD	Mean	SD	ANF	CNC
Crack sealing (%)									
developed in geothermal water	1 month	21.44	20	36.78	7.58	46.74	10.72	72	118
	3 months	42.08	37.93	72.08	13.10	91.58	12.11	71	118
	6 months	51.17	46.12	87.66	17.45	100	0	71	95
Healing efficiency (%)									
developed in geothermal water	1 month	29.9	21.2	35.6	19.8	45.0	18.2	19	51
	3 months	55.5	32.7	69.9	25.8	84.5	19.3	26	52
	6 months	63.1	24.5	87.1	29.9	97.1	28.9	38	54

Note: SD = standard deviation.

considerably enhanced the self-healing capacity of fiber-reinforced cementitious composites, in terms of both recovery of waterproofing and self-repair of the crack.

All the main parameters obtained from the tests are presented in Tables 6 and 7. Table 6 presents the cumulative results of all UHPFRC mixes before healing, whereas Table 7 presents the cumulative results of all UHPFRC mixes after healing. The performance improvement with nanoaditives also is indicated. The presence of nanoadditions had very positive results in terms of performance, especially in terms of crack sealing and healing efficiency (Tables 6 and 7).

Conclusions

This paper evaluated the intrinsic durability characteristics and the durability in the cracked state (self-healing capacity) of UHPFRC mixes containing a high amount of GGBS together with crystalline admixtures as a self-healing stimulator and alumina nanofibers and cellulose nanocrystals as functionalizing nanoconstituents. The following conclusions were reached:

- An increase of flexural strengths due to nanoconstituents was detected when specimens were immersed in geothermal water, especially the mix with cellulose nanocrystals, which likely was due to the hydration-stimulating effects of the nanoconstituents, which likely also may hinder the negative effects of aggressive ions in the curing water.
- The higher portlandite and bound water contents in the UHDC with nanoconstituents had beneficial effects on the hydration of cement; more portlandite was detected with CNC and ANF. A very dense cement paste with a significant decrease of microcracking generation in cement paste was found when nanoconstituents were added.
- The addition of nanoconstituents CNF and ANF to the reference UHDC led to a high-density cement paste, with a more refined pore structure with a significant decrease in total porositynano.
- The nanoconstituents significantly contributed to reducing the autogenous and drying shrinkage. The mix with cellulose nanocrystals had the lowest autogenous shrinkage, due to the internal curing potential of the nanocellulose.
- Chloride migration coefficients always were lower than 10×10^{-13} m^2/s, indicating a low permeability of chloride ions for all the investigated mixes.
- Low water absorption was found for all the UHDCs investigated, although some CNC concretes weremore prone to water capture.
- Nanoconstituents considerably improved the self-healing capacity of fiber-reinforced cementitious composites immersed in geothermal water, in terms of both recovery of waterproofing (crack sealing) and self-repair of cracks (crack healing), for all healing periods.

Data Availability Statement

All data, models, and code generated or used during the study appear in the published article.

Acknowledgments

The research activity reported in this paper has been performed in the framework of the ReSHEALience project (Rethinking coastal defence and green-energy Service infrastructures through enHancEd-durAbiLity high-performance cement-based materials) which has received funding from the European Union's Horizon 2020 research and innovation program under Grant Agreement No. 760824. The collaboration of ReSHEALience partners ANF-Development, API-Europe, and Penetron Italia in supplying alumina nanofibers, cellulose nanofibrils and crystals, and the crystalline self-healing promoter, respectively, is acknowledged. The authors thank BuzziUnicem, Azichem, and BASF Italia for supplying of cement, steel fibers, and superplasticizer, respectively, used for casting the different investigated UHPFRC mixes.

References

ACI (American Concrete Institute). 2010. *Report on chemical admixtures for concrete*. ACI 212-3R-10. Farmington Hills, MI: ACI.

Alonso, C., C. Andrade, E. Menéndez, and E. Gayo. 2005. "Microstructural changes in high and ultra high strength concrete exposed to high temperature environments." *ACI Int. Spec. Publ.* 229 (Sep): 289–302.

Barnat-Hunek, D., M. Szymanska-Chargot, M. Jarosz-Hadam, and G. Lagód. 2019. "Effect of cellulose nanofibrils and nanocrystals on physical properties of concrete." *Constr. Build. Mater.* 223 (Oct): 1–11. https://doi.org/10.1016/j.conbuildmat.2019.06.145.

Baroghel-Bouny, V. 2004. "Which toolkit for durability evaluation as regards chloride ingress into concrete? Part II: Development of a performance approach based on durability indicators and monitoring parameters." In *Proc., 3rd Int. RILEM Workshop on Testing and Modelling Chloride Ingress into Concrete*. Paris: RILEM Publications. https://doi.org/10.1617/2912143578.009.

Borg, R. P., E. Cuenca, E. M. Gastaldo Brac, and L. Ferrara. 2018. "Crack sealing capacity in chloride-rich environments of mortars containing

different cement substitutes and crystalline admixtures." *J. Sustainable Cem.-Based Mater.* 7 (3): 141–159. https://doi.org/10.1080/21650373.2017.1411297.

Cao, Y., P. Zavaterri, J. Youngblood, R. Moon, and J. Weiss. 2015. "The influence of cellulose nanocrystal additions on the performance of cement paste." *Cem. Concr. Compos.* 56 (Feb): 73–83. https://doi.org/10.1016/j.cemconcomp.2014.11.008.

CEN (European Committee for Standardization). 2002a. *Products and systems for the protection and repair of concrete structures – Test methods – Determination of resistance of capillary absorption*. EN 13057. Brussels, Belgium: CEN.

CEN (European Committee for Standardization). 2002b. *Products and systems for the protection and repair of concrete structures – Test methods – Part 4: Determination of shrinkage and expansion*. EN 12617-4. Brussels, Belgium: CEN.

CEN (European Committee for Standardization). 2006. *Testing concrete in structures—Part 4: Determination of ultrasonic pulse velocity*. EN 12504-4. Brussels, Belgium: CEN.

CEN (European Committee for Standardization). 2019. *Testing hardened concrete Part 11: Determination of the chloride resistance of concrete, unidirectional diffusion*. CEN 12390-11. Brussels, Belgium: CEN.

CEN (European Committee for Standardization). 2020. *Methods of test for mortar for masonry. Part II: Determination of flexural and compressive strength of hardened mortar*. EN 1015-11-1999. Brussels, Belgium: CEN.

Chen, Y., T. Ji, Z. Yang, W. Zhan, and Y. Zhang. 2020. "Sustainable use of ferronickel slag in cementitious composites and the effect on chloride penetration resistance." *Constr. Build. Mater.* 240 (Apr): 117969. https://doi.org/10.1016/j.conbuildmat.2019.117969.

Claramunt, J., H. Ventura, R. Toledo-Filho, and M. Ardanuy. 2019. "Effect of nanocelluloses on the microstructure and mechanical performance of CAC cementitious matrices." *Cem. Concr. Res.* 119 (May): 64–76. https://doi.org/10.1016/j.cemconres.2019.02.006.

Cuenca, E., L. D'Ambrosio, D. Lizunov, A. Tretjakov, O. Volobujeva, and L. Ferrara. 2021a. "Mechanical properties and self-healing capacity of ultra high performance fibre reinforced concrete with alumina nanofibres: Tailoring ultra high durability concrete for aggressive exposure scenarios." *Cem. Concr. Compos.* 118 (Apr): 103956. https://doi.org/10.1016/j.cemconcomp.2021.103956.

Cuenca, E., F. Lo Monte, M. Moro, A. Schiona, and L. Ferrara. 2021b. "Effects of autogenous and stimulated self-healing on durability and mechanical performance of UHPFRC: Validation of tailored test method through multi-performance healing-induced recovery indices." *Sustainability* 13 (20): 11386. https://doi.org/10.3390/su132011386.

Cuenca, E., A. Mezzena, and L. Ferrara. 2021c. "Synergy between crystalline admixtures and nano-constituents in enhancing autogenous healing capacity of cementitious composites under cracking and healing cycles in aggressive waters." *Constr. Build. Mater.* 266 (Jan): 121447. https://doi.org/10.1016/j.conbuildmat.2020.121447.

Cuenca, E., S. Rigamonti, E. Gastaldo Brac, and L. Ferrara. 2021d. "Crystalline admixture as healing promoter in concrete exposed to chloride-rich environments: Experimental study." *ASCE J. Mater. Civ. Eng.* 33 (3): 04020491. https://doi.org/10.1061/%28ASCE%29MT.1943-5533.0003604.

Cuenca, E., A. Tejedor, and L. Ferrara. 2018. "A methodology to assess crack-sealing effectiveness of crystalline admixtures under repeated cracking-healing cycles." *Constr. Build. Mater.* 179 (Aug): 619–632. https://doi.org/10.1016/j.conbuildmat.2018.05.261.

Darquennes, A., K. Olivier, F. Benboudjema, and R. Gagné. 2016. "Self-healing at early-age, a way to improve the chloride resistance of blast-furnace slag cementitious materials." *Constr. Build. Mater.* 113 (Jun): 1017–1028. https://doi.org/10.1016/j.conbuildmat.2016.03.087.

Fernández, A., J. L. G. Calvo, and M. C. Alonso. 2018. "Ordinary portland cement composition for the optimization of the synergies of supplementary cementitious materials of ternary binders in hydration processes." *Cem. Concr. Compos.* 89 (May): 238–250. https://doi.org/10.1016/j.cemconcomp.2017.12.016.

Ferrara, L., et al. 2018. "Experimental characterization of the self-healing capacity of cement based materials and its effects on the material performance: A state of the art report by COST Action SARCOS WG2." *Constr. Build. Mater.* 167 (Apr): 115–142. https://doi.org/10.1016/j.conbuildmat.2018.01.143.

Ferrara, L., et al. 2019. "An overview on H2020 project 'ReSHEALience'." In *Proc., IABSE Symp.* Red Hook, NY: Curran Associates.

Ferrara, L., V. Krelani, and M. Carsana. 2014. "A 'fracture testing' based approach to assess crack healing of concrete with and without crystalline admixtures." *Constr. Build. Mater.* 68 (Oct): 535–551. https://doi.org/10.1016/j.conbuildmat.2014.07.008.

Gopalakrishnan, R., and R. Jeyalakshmi. 2018. "Strength deterioration of nano-silica contained in ordinary Portland cement concretes in aggressive sulfate environments." *Eur. Phys. J. Plus* 133 (351): 1–19. https://doi.org/10.1140/epjp/i2018-12162-3.

Hassan, A. M. T., and S. W. Jones. 2012. "Non-destructive testing of ultra high performance fibre reinforced concrete (UHPFRC): A feasibility study for using ultrasonic and resonant frequency testing techniques." *Constr. Build. Mater.* 35 (Oct): 361–367. https://doi.org/10.1016/j.conbuildmat.2012.04.047.

Hisseine, O., N. Soliman, B. Tolnai, and A. Tagnit-Hamou. 2020. "Nano-engineered ultra-high performance concrete for controlled autogenous shrinkage using nanocellulose." *Cem. Concr. Res.* 137 (Nov): 106217. https://doi.org/10.1016/j.cemconres.2020.106217.

ISO. 2016. *Evaluation of pore size distribution and porosity of solid materials by mercury porosimetry and gas adsorption—Part 1: Mercury porosimetry*. ISO 15901-1:2016. Geneva: ISO.

Kawashima, S., and S. Shah. 2011. "Early-age autogenous and drying shrinkage behavior of cellulose fiber-reinforced cementitious materials." *Cem. Concr. Compos.* 33 (2): 201–208. https://doi.org/10.1016/j.cemconcomp.2010.10.018.

Kayali, O., M. S. H. Khan, and M. S. Ahmed. 2012. "The role of hydrotalcite in chloride binding and corrosion protection in concretes with ground granulated blast furnace slag." *Cem. Concr. Compos.* 34 (8): 936–945. https://doi.org/10.1016/j.cemconcomp.2012.04.009.

Kumar, S., R. Kumar, A. Bandopadhyay, T. Alex, B. Ravi Kumar, S. Das, and S. Mehrotra. 2008. "Mechanical activation of granulated blast furnace slag and its effect on the properties and structure of portland slag cement." *Cem. Concr. Compos.* 30 (8): 679–685. https://doi.org/10.1016/j.cemconcomp.2008.05.005.

Kusumawardaningsih, Y., E. Fehling, M. Ismail, A. Amen, and M. Aboubakr. 2015. "Tensile strength behavior of UHPC and UHPFRC." *Procedia Eng.* 125 (Jan): 1081–1086. https://doi.org/10.1016/j.proeng.2015.11.166.

Lee, H.-J., S.-K. Kim, H.-S. Lee, and W. Kim. 2019. "A study on the drying shrinkage and mechanical properties of fiber reinforced cement composites using cellulose nanocrystals." *Int. J. Concr. Struct. Mater.* 13 (1): 1–11. https://doi.org/10.1186/s40069-019-0351-2.

Lee, S.-J., S. Kawashima, K.-J. Kim, S.-K. Woo, and J.-P. Won. 2018. "Shrinkage characteristics and strength recovery of nanomaterials-cement composites." *Compos. Struct.* 202 (Oct): 559–565. https://doi.org/10.1016/j.compstruct.2018.03.003.

Li, K., and L. Li. 2019. "Crack-altered durability properties and performance of structural concretes." *Cem. Concr. Res.* 124 (Oct): 105811. https://doi.org/10.1016/j.cemconres.2019.105811.

Li, Z., H. Wang, S. He, Y. Lu, and M. Wang. 2006. "Investigations on the preparation and mechanical properties of the nano-alumina reinforced cement composite." *Mater. Lett.* 60 (3): 356–359. https://doi.org/10.1016/j.matlet.2005.08.061.

Lo Monte, F., and L. Ferrara. 2020. "Tensile behaviour identification in ultra-high performance fibre reinforced cementitious composites: Indirect tension tests and back analysis of flexural test results." *Mater. Struct.* 53 (6): 1–12. https://doi.org/10.1617/s11527-020-01576-8.

Luna, F. J., Á. Fernández, and M. C. Alonso. 2018. "The influence of curing and aging on chloride transport through ternary blended cement concrete." *Mater. Constr.* 68 (332): e171. https://doi.org/10.3989/mc.2018.11917.

Maes, M., D. Snoeck, and N. De Belie. 2016. "Chloride penetration in cracked mortar and the influence of autogenous crack healing." *Constr. Build. Mater.* 115 (Jul): 114–124. https://doi.org/10.1016/j.conbuildmat.2016.03.180.

Muzenski, S., I. Flores-Vivian, and K. Sobolev. 2019. "Ultra-high strength cement-based composites designed with aluminum oxide nano-fibers."

Constr. Build. Mater. 220 (Sep): 177–186. https://doi.org/10.1016/j.conbuildmat.2019.05.175.

Nordtest. 1999. *Concrete, mortar and cement-based repair materials: Chloride migration coefficient from non-steady-state migration experiments*. NT BUILD 492. Espoo, Finland: Nordtest.

Nordtest. 2015. *Hydrophobic impregnation for concrete prevention of chloride ingress-filter effect*. NT515. Espoo, Finland: Nordtest.

Ozbay, E., M. Erdermir, and H. Durmus. 2016. "Utilization and efficiency of ground granulated blast furnace slag on concrete properties—A review." *Constr. Build. Mater.* 105 (Feb): 423–434. https://doi.org/10.1016/j.conbuildmat.2015.12.153.

Sánchez, F., and K. Sobolev. 2010. "Nanotechnology in concrete—A review." *Constr. Build. Mater.* 24 (11): 2060–2071. https://doi.org/10.1016/j.conbuildmat.2010.03.014.

Shi, C., Z. Wu, J. Xiao, D. Wang, Z. Huang, and Z. Fang. 2015. "A review on ultra high performance concrete: Part I. Raw materials and mixture design." *Constr. Build. Mater.* 101 (Dec): 741–751. https://doi.org/10.1016/j.conbuildmat.2015.10.088.

Sisomphon, K., O. Copuroglu, and E. A. B. Koenders. 2012. "Self-healing of surface cracks in mortars with expansive additive and crystalline additive." *Cem. Concr. Compos.* 34 (4): 566–574. https://doi.org/10.1016/j.cemconcomp.2012.01.005.

Snoeck, D., P. Van den Heede, T. Van Mullem, and N. De Belie. 2018. "Water penetration through cracks in self-healing cementitious materials with superabsorbent polymers studied by neutron radiography." *Cem. Concr. Res.* 113 (Nov): 86–98. https://doi.org/10.1016/j.cemconres.2018.07.002.

Sobolev, K. 2016. "Modern developments related to nanotechnology and nanoengineering of concrete." *Front. Struct. Civ. Eng.* 10 (2): 131–141. https://doi.org/10.1007/s11709-016-0343-0.

Soin, A. V., L. J. J. Catalan, and S. D. Kinrade. 2013. "A combined QXRD/TG method to quantify the phase composition of hydrated Portland cements." *Cem. Concr. Res.* 48 (Jun): 17–24. https://doi.org/10.1016/j.cemconres.2013.02.007.

UNE (Spanish Association for Standardization). 2008. *Concrete durability. Test methods. Determination of the capillar suction in hardened concrete. Fagerlund method*. UNE 83982. Madrid, Spain: UNE.

UNE (Spanish Association for Standardization). 2008. *Concrete durability. Test methods. Determination of the electrical resistivity. Part 1: Direct test*. UNE 83988-1. Madrid, Spain: UNE.

Van Belleghem, B., P. Van den Heede, K. Van Tittelboom, and N. De Belie. 2017. "Quantification of the service life extension and environmental benefit of chloride exposed self-healing concrete." *Materials* 10 (1): 5. https://doi.org/10.3390/ma10010005.

Wang, W., J. Liu, F. Agostini, C. A. Davy, F. Skoczylas, and D. Corvez. 2014. "Durability of an ultra high performance fiber reinforced concrete (UHPFRC) under progressive aging." *Cem. Concr. Res.* 55 (Jan): 1–13. https://doi.org/10.1016/j.cemconres.2013.09.008.

Wu, Z., C. Shi, K. H. Khayat, and S. Wan. 2016. "Effects of different nanomaterials on hardening and performance of ultra-high strength concrete (UHSC)." *Cem. Concr. Compos.* 70 (Jul): 24–34. https://doi.org/10.1016/j.cemconcomp.2016.03.003.

Yang, L., C. Shi, and Z. Wu. 2019. "Mitigation techniques for autogenous shrinkage of ultra-high-performance concrete—A review." *Composites, Part B* 178 (Dec): 107456. https://doi.org/10.1016/j.compositesb.2019.107456.

Zhang, W., Q. Zheng, A. Ashour, and B. Han. 2020. "Self-healing cement concrete composites for resilient infrastructures: A review." *Composites, Part B* 189 (May): 107892. https://doi.org/10.1016/j.compositesb.2020.107892.

Zhang, Y., W. Zhang, W. She, L. Ma, and W. Zhu. 2012. "Ultrasound monitoring of setting and hardening process of ultra-high performance cementitious materials." *NDT & E Int.* 47 (Apr): 177–184. https://doi.org/10.1016/j.ndteint.2009.10.006.